Topological Eigenvalue Braiding and Quantum State Transfer Near a Third-Order Exceptional Point

Citation for the original published paper (version of record):
Zhang, H., Liu, T., Xiang, Z. et al (2025). Topological Eigenvalue Braiding and Quantum State Transfer Near a Third-Order Exceptional Point. PRX Quantum, 6(2).
http://dx.doi.org/10.1103/PRXQuantum.6.020328

(article starts on next page)

Topological Eigenvalue Braiding and Quantum State Transfer Near a Third-Order Exceptional Point

He Zhang,[1,2,*] Tong Liu,[1,3,*,†] Zhongcheng Xiang,[1,2,4,5,6,7] Kai Xu,[1,2,4,5,6,7] Heng Fan,[1,2,4,5,6,7] and Dongning Zheng[1,2,5,6,7]

[1] Institute of Physics, Chinese Academy of Sciences, Beijing 100190, China
[2] School of Physical Sciences, University of Chinese Academy of Sciences, Beijing 100190, China
[3] Department of Microtechnology and Nanoscience, Chalmers University of Technology, Gothenburg 41296, Sweden
[4] Beijing Academy of Quantum Information Sciences, Beijing 100193, China
[5] Hefei National Laboratory, Hefei 230088, China
[6] CAS Center of Excellence for Topological Quantum Computation, University of Chinese Academy of Sciences, Beijing 100190, China
[7] Songshan Lake Materials Laboratory, Dongguan, Guangdong 523808, China

(Received 23 January 2025; revised 8 April 2025; accepted 22 April 2025; published 9 May 2025)

Non-Hermitian systems exhibit a variety of unique features rooted in the presence of exceptional points (EPs). The distinct topological structure in the proximity of an EP gives rise to counterintuitive behaviors absent in Hermitian systems, which emerge after encircling the EP either quasistatically or dynamically. However, experimental exploration of EP encirclement in quantum systems, particularly those involving high-order EPs, remains challenging due to the difficulty of coherently controlling more degrees of freedom. In this work, we experimentally investigate the eigenvalue braiding and state transfer arising from the encirclement of EP in a three-dimensional non-Hermitian quantum system using superconducting circuits. We characterize the second- and third-order EPs through the coalescence of eigenvalues. Then we reveal the topological structure near the EP3 by quasistatically encircling it along various paths with three independent parameters, which yields the eigenvalue braiding described by the braid group B_3. Additionally, we observe chiral state transfer between three eigenstates under a fast driving scheme when no EPs are enclosed, while time-symmetric behavior occurs when at least one EP is encircled. Our findings offer insights into understanding non-Hermitian topological structures and the manipulation of quantum states through dynamic operations.

DOI: 10.1103/PRXQuantum.6.020328

I. INTRODUCTION

The exploration of non-Hermitian systems has uncovered a wide range of intriguing phenomena, such as unidirectional invisibility [1,2], perfect absorption [3,4], lasing effects [5–7], frequency combs [8], and unconventional beam dynamics [9]. These findings are fostered by the presence of non-Hermitian degeneracies known as kth-order exceptional points (EPks), where k eigenvalues and their corresponding eigenstates both simultaneously coalesce. The nontrivial topological structure near an EP within the Riemann manifold leads to unique behaviors that have no counterpart in Hermitian systems.

In an N-dimensional non-Hermitian system, traversing a directional control loop parametrized by s around an EP in a quasistatic manner results in a permutation of N complex eigenvalues $\{\lambda_i(s)\}$ [10,11]. The trajectories of eigenvalues in the three-dimensional space $(\mathrm{Re}[\lambda], \mathrm{Im}[\lambda], s)$ resemble N intertwined strands of a braid. For the EPs in a two-dimensional non-Hermitian system, the topology of control loops in a two-dimensional parameter space can be classified by the group $\mathbb{Z}$, which also corresponds to the braid degree of two eigenvalues along the loop [12].

To predict the evolution of N eigenvalues, however, it is necessary to account for the topological structure of the space $\mathcal{G}_N$, excluding degenerate points in a higher-dimensional parameter space of $2(N-1)$ dimensions [13].

[*] These authors contributed equally to this work.
[†] Contact author: liutong181@mails.ucas.ac.cn

A bijection can be established between the fundamental group of the space $\mathcal{G}_N$ and the Artin braid group B_N [14–16], which is a non-Abelian group for $N > 2$. In the case of $N = 3$, the full parameter space is four-dimensional, with all EPs forming a two-dimensional space isomorphic to a cone of the trefoil knot $\mathcal{K} \times \mathbb{R}_{>0}$ where $\mathcal{K}$ denotes the trefoil knot [17]. To locate the EP3 and ascertain the braid relation, four independent parameters must be adjusted, which demands substantial experimental effort [17]. Recent studies suggest that additional symmetries can lessen the degrees of freedoms required to observe high-order EPs [18,19]. Therefore, it remains to be explored whether digesting the topology of encircling EPs and reproducing the associated braid group B_N still necessitates $2(N-1)$ parameters when such symmetries are present.

Another noteworthy phenomenon is the mode switch among eigenstates induced by the dynamical encirclement of EPs. Instead of the eigenstate exchange observed in quasistatic encirclement, nonadiabatic transitions during the dynamical cycle lead to the breakdown of the adiabatic theorem [20–24]. The final state is determined by the encirclement direction and the location of the starting point, irrespective of the initial state. While such novel behaviors have been demonstrated in classical systems [25–31], extending this topological control to quantum systems demands both high controllability and long coherence time. Although recent studies have realized the dynamical encirclement of a second-order EP in real quantum systems [32,33], the exploration of higher-order EP remains elusive due to the challenge of precisely controlling more time-dependent parameters. Moreover, the chiral state transfer can occur even in the absence of encircled EPs [31,33,34], which has yet to be observed in high-dimensional non-Hermitian systems.

In this work, we investigate eigenvalue braiding and state transfer in a three-dimensional non-Hermitian quantum system comprising a transmon coupled with a microwave resonator. Leveraging the multilevel structure of transmon, we approximate it as a three-level quantum system and achieve tunable coupling between the transmon and the resonator. Dissipation is introduced by the resonator, which undergoes much faster photon decay compared to the transmon [35–37]. We identify the EP2s and EP3 in this system by the coalescence of eigenvalues. We develop a mapping between the control loop and the braid of eigenvalues, and illustrate how to employ this mapping to generate the complete braid group B_3 with three parameters. We reveal that both time-symmetric and chiral state transfers can appear by choosing different paths for the dynamical encirclement of EPs, which can be implemented through a rapid driving scheme. The chiral state transfer manifests only when no EPs are surrounded.

II. SYMMETRY-ENABLED REALIZATION OF HIGH-ORDER EPS

We construct a non-Hermitian system on a superconducting quantum processor with a transmon and a capacitively coupled microwave resonator. Figure 1(a) illustrates the processor utilized in our experiment, which contains a one-dimensional array of ten frequency-tunable transmon elements. We only exploit Q_{10} in the experiment, while the others are detuned from the experimental frequency using magnetic flux bias to reduce crosstalk. The transmon Q_{10} can be regarded as a qutrit comprising its ground state $|g\rangle$, the first excited state $|e\rangle$, and the second excited state $|f\rangle$, with an energy relaxation time of $T_e = 48$ μs and $T_f = 35$ μs. The initial state preparation and readout are operated at the sweet-spot frequencies $\omega_{ge} = 2\pi \times 5.684$ GHz and $\omega_{ef} = \omega_{ge} + \alpha = 2\pi \times 5.431$ GHz with an anharmonicity $\alpha/2\pi = -253$ MHz. The transitions between g-e and e-f are individually addressed by different modulated microwave pulses generated by arbitrary waveform generators (AWGs). The transmon is coupled with the strength $J/2\pi = 48$ MHz to a readout resonator of frequency $\omega_r/2\pi = 6.697$ GHz. The photon decay rate κ of resonator is measured to be 5 MHz by the ac Stark effect [38].

Although the coupling strength J is fixed by the geometry of the device, cavity-assisted Raman process enables a controllable effective coupling G between $|g,1\rangle$ and $|f,0\rangle$ by employing a coherent microwave drive where $|s,n\rangle$ denotes the product state of the transmon in state $|s\rangle$ and the resonator in the n photon Fock state $|n\rangle$ [35–37]. By applying an additional Rabi drive between the $|e,0\rangle$ and $|f,0\rangle$ states, the dynamics of the coupled system in the subspace spanned by the $|e,0\rangle$, $|f,0\rangle$, and $|g,1\rangle$ states is governed by the non-Hermitian Hamiltonian

$$H = \begin{pmatrix} -\delta_{ef} & \Omega & 0 \\ \Omega & 0 & G \\ 0 & G & -i\kappa/2 \end{pmatrix}, \qquad (1)$$

where δ_{ef} is the drive detuning, accounting for the ac Stark shift induced by the $f0$-$g1$ drive, and Ω is the drive amplitude between the $|e,0\rangle$ and $|f,0\rangle$ states. For simplicity, Ω and G are both tuned to be real. The ac Stark shift for the $|g,1\rangle$ state induced by the $f0$-$g1$ drive is consistently compensated for in the experiment.

The non-Hermitian Hamiltonian in Eq. (1) can be parameterized with three real independent variables (δ_{ef}, Ω, G), which can be accurately mapped onto the raw instrument parameters following a series of calibrations prior to the experiment. However, the existence of EPks generally necessitate $2(k-1)$ constraints implying that at least four free parameters are required to investigate EP3s [17,18,39]. To resolve this discrepancy, we mention that the Hamiltonian possesses

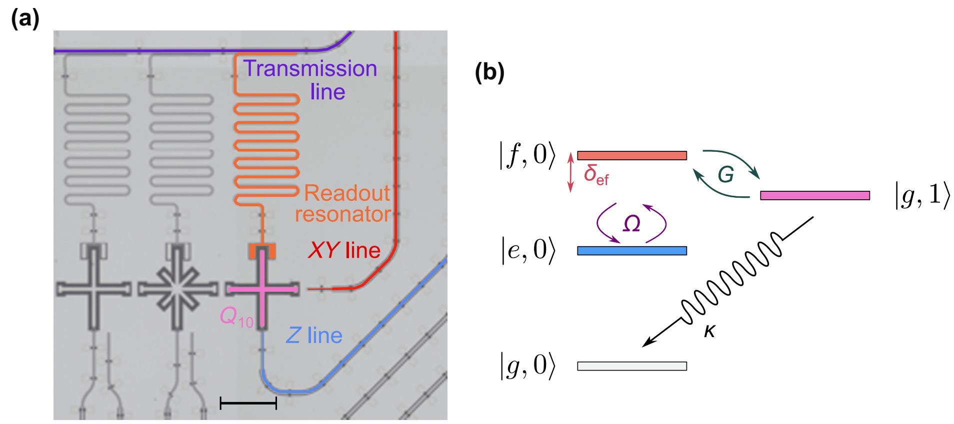

FIG. 1. Three-level non-Hermitian systems. (a) The optical picture of the ten-qubit superconducting quantum processor with highlighting circuit elements of a transmon and its attached resonator. Scale bar at the bottom, 0.2 mm. (b) The non-Hermitian system is composed of the states $|e,0\rangle$, $|f,0\rangle$, and $|g,1\rangle$, with dissipation irreversibly driving the transition from $|g,1\rangle$ to $|g,0\rangle$.

a pseudochirality at $\delta_{ef}=0$, which lowers the number of constraints to two [40,41]. Therefore, we can observe an isolated EP3 at the two-dimensional surface $\delta_{ef}=0$ in the parameter space. To explicitly demonstrate it, we consider the characteristic polynomial of the Hamiltonian $\varphi_\lambda(H)=\lambda^3+(\delta_{ef}+i\kappa/2)\lambda^2-(G^2+\Omega^2-i\kappa\delta_{ef}/2)\lambda-(G^2\delta_{ef}+i\kappa\Omega^2/2)$. The roots of this cubic polynomial yield three eigenvalues λ_1, λ_2, and λ_3. All of them can be expressed as $(-\frac{p}{2}+\sqrt{\Delta})^{1/3}\alpha+(-\frac{p}{2}-\sqrt{\Delta})^{1/3}\alpha^*-(\delta_{ef}+i\frac{\kappa}{2})/3$ where α takes the value from $\{1,e^{i2\pi/3},e^{i4\pi/3}\}$ using Cardano's formula. Here, Δ denotes the discriminant of $\varphi_\lambda(H)$, and p is a function about δ_{ef}, Ω, and G. The square root of Δ indicates that EP2s emerge at $\Delta=0$ and coalesce into an EP3 when $p=0$ as well. We plot the EP2s and EP3 in the first quadrant of the plane $\delta_{ef}=0$ in Fig. 2(a). The boundary lines of the shaded region $\Delta<0$ consist of two branches of EP2s, and EP3 is located at the cusp of order-2 exceptional arcs. In addition, the system preserves an anti-PT symmetry at $\delta_{ef}=0$ [42–46]. The sign change of Δ characterizes an anti-PT-symmetry phase transition. In the symmetry-unbroken regime ($\Delta<0$), all eigenvalues are purely imaginary, leading to exponential decay dynamics. Spontaneous symmetry breaking occurs at EP2s ($\Delta=0$), where two eigenvalues degenerate. When $\Delta>0$, the eigenvalues become complex and result in damped oscillations.

We experimentally examine EPs along three distinct routines that traverse exceptional arcs with two, one, and zero crossings on the plane $\delta_{ef}=0$, as shown in Fig. 2(a). We fix the Rabi driving amplitude Ω between the $|e,0\rangle$ and $|f,0\rangle$ states while gradually increasing the amplitude of $f0$-$g1$ driving pulse. Simultaneously, we adjust the driving frequency to maintain zero detuning. For each point on the trajectories, we prepare the initial state as $(|e,0\rangle-i|f,0\rangle)/\sqrt{2}$ and measure the evolution of the probabilities for the three qutrit states $|g\rangle$, $|e\rangle$, and $|f\rangle$. The retrieved eigenvalues are obtained from the non-Hermitian Hamiltonian using the extracted experiment parameters $(\delta_{ef}^{\mathrm{exp}},\Omega^{\mathrm{exp}},G^{\mathrm{exp}})$. These parameters are determined by fitting the population dynamics of three states simultaneously (see Appendix B).

Figures 2(b)–2(d) present the retrieved eigenvalues corresponding to the three specific routines shown in Fig. 2(a), respectively. All experiment data align well with the theoretic predictions. In Fig. 2(b), one eigenvalue remains purely imaginary while the other two are symmetrically mirrored about the plane $\mathrm{Re}[\lambda]=0$ as G increases, before converging at the first EP2 (EP2a) in the left branch. Up crossing EP2a, all eigenvalues turn imaginary until they reach another EP2 (EP2b) in the right branch. Passing through the symmetry-unbroken region, two eigenvalues become complex again. The real part of the eigenvalues undergoes pitchfork bifurcations at two EP2s, as depicted on the projected plane in Fig. 2(b). Notably, the symmetric eigenvalues after crossing EP2b are distinct from the pair before crossing EP2a as illustrated in Fig. 2(b), which gives rise to two types of eigenvalue braiding when encircling EP2s in different branches. Next, we follow the blue routine where $\Omega/\kappa=3^{-3/2}/2$ and encounter the EP3 at $G/\kappa=(2/3)^{3/2}/2$. Figure 2(c) plots the eigenvalues in the vicinity of EP3 where all three eigenvalues coalesce, confirming the existence of EP3. The inner projected plane also shows the merging of two bifurcations points into one. In contrast, for the green routine without intersecting the region where $\Delta<0$, no eigenvalues coalescence is observed in Fig. 2(d) as anticipated.

III. COMPLEX EIGENVALUE BRAIDING

After identifying EPs on the surface $\delta_{ef}=0$, we investigate the behavior of eigenvalues by varying the parameters of H around a loop in the parameter space. Contrary to

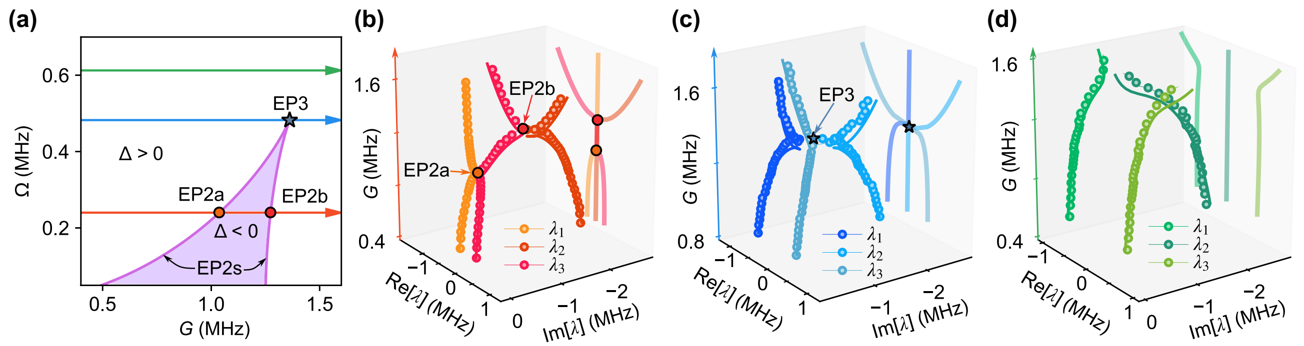

FIG. 2. Determine EP2s and EP3. (a) The phase diagram in the first quadrant of the plane $\delta_{ef} = 0$. Purple arcs represent EP2s and the blue star denotes the EP3. The colored region surrounded by EP2s represents the anti-PT-symmetry-broken phase with discriminant $\Delta < 0$. Red, blue, and red arrows represent specific routines. (b)–(d) Retrieved eigenvalues corresponding to the routines in (a). Dots are experimental data and solid lines are theoretic results. The standard error of the mean in the measured data is no larger than the size of the plotted points. The solid lines on the projected planes show the real parts of the eigenvalues.

the requirement of a four-dimensional parameter space [17], we demonstrate that three independent parameters are sufficient to realize the entire braid group B_3. Figure 3(a) illustrates EPs within the three-dimensional parameter space. We focus on the EPs depicted by the blue solid lines, which continue infinitely in the parameter space as $|\delta_{ef}|$ increases, rather than constituting a closed knot [17]. Two additional exceptional lines, defined by $\{(\delta_{ef}, \Omega, G)|\Omega = 0, G = \pm\kappa/4\}$, are not joined with the main framework of EPs and are not shown in the figure, as they do not impact our results. Owing to the absence of the coupling between $|e, 0\rangle$ and $|g, 1\rangle$, the eigenvalues are invariant regardless of the phase variations or the signs of Ω and G (see Appendix A). Consequently, the EPs shown in the first quadrant of the surface $\delta_{ef} = 0$ [Fig. 2(a)] extend to four quadrants in Fig. 3(a).

To observe the spectral flow, we select five control loops which share a common base point serving as both start and end points, as shown in Fig. 3(a). The details of these control loops are provided in Appendix C. For clarity, the control loops in green, purple, and brown are symmetrically mirrored in the other quadrants. The five loops belonging to different homotopy classes give rise to different braids of eigenvalues in Figs. 3(b)–3(f), where the evolution of each eigenvalue resembles a strand. The red and blue loops encircling distinct branches of EP2s on the surface $\delta_{ef} = 0$ generate elements σ_1 and σ_2 of the braid group B_3, respectively. By concatenating these loops, we can derive any element in B_3, such as σ_1^2, $\sigma_2\sigma_1$, and $\sigma_1\sigma_2$ [Figs. 3(d)–3(f)]. As illustrated in Figs. 3(e) and 3(f), the braids formed by concatenating σ_1 and σ_2 in opposite orders are not equivalent, verifying that B_3 is a non-Abelian group. Apart from the decomposition into red and blue loops, the purple or brown loop can also be interpreted as a concatenation of loops encircling the other two exceptional arcs with $\delta_{ef} \neq 0$. The equivalence of two concatenations leads to the braid identity $\sigma_1\sigma_2\sigma_1 = \sigma_2\sigma_1\sigma_2$, which is also known as the Yang-Baxter equation (see Appendix L) [47]. From another prospective, the purple and brown loops can be continuously deformed into the loops around EP3 without concatenation, producing a full braid of three eigenvalues in one step. Similarly, the red and blue loops can be viewed as encircling EP3 within a plane, which separates one exceptional arc from the other three, producing a braid between two eigenvalues. These results indicate the anisotropy of EP3 stemming from the novel geometry of the space $\mathcal{G}_N$ (see Appendix K) [39].

We mention that such a topological structure close to the EP3 cannot be fully characterized by the discriminant number $\nu = \sum_{i\neq j} \nu_{ij}$, where ν_{ij} is the vorticity invariant between eigenvalues λ_i and λ_j [48,49]. It can be verified that $\nu = -1$ for the loops shown in Figs. 3(b)–3(c) and $\nu = -2$ for the loops shown in Figs. 3(d)–3(f). Another promising topological invariant is the knot invariant, obtained by connecting the corresponding ends of the braid to form a knot or link [12,16]. However, different braids may yield the same knot or link, as seen in Figs. 3(b) and 3(c), where both braids give rise to the same unlink, making them indistinguishable by knot invariants. Therefore, the braid group is a more fundamental tool for a comprehensive understanding of the topological structure near a high-order EP.

IV. CHIRAL QUANTUM STATE TRANSFER

We now turn to the case of dynamically varying parameters along a cycle, where only one eigenstate dominates at the end of the evolution. In a two-dimensional non-Hermitian system, if a loop produces one eigenstate and its reverse yields the other one, it is called chiral-state transfer; otherwise, it is termed time-symmetric state transfer. In higher-dimensional systems, this process is more intricate due to the presence of more eigenstates and EPs. To investigate the impact of EP on state transfer, we confine the

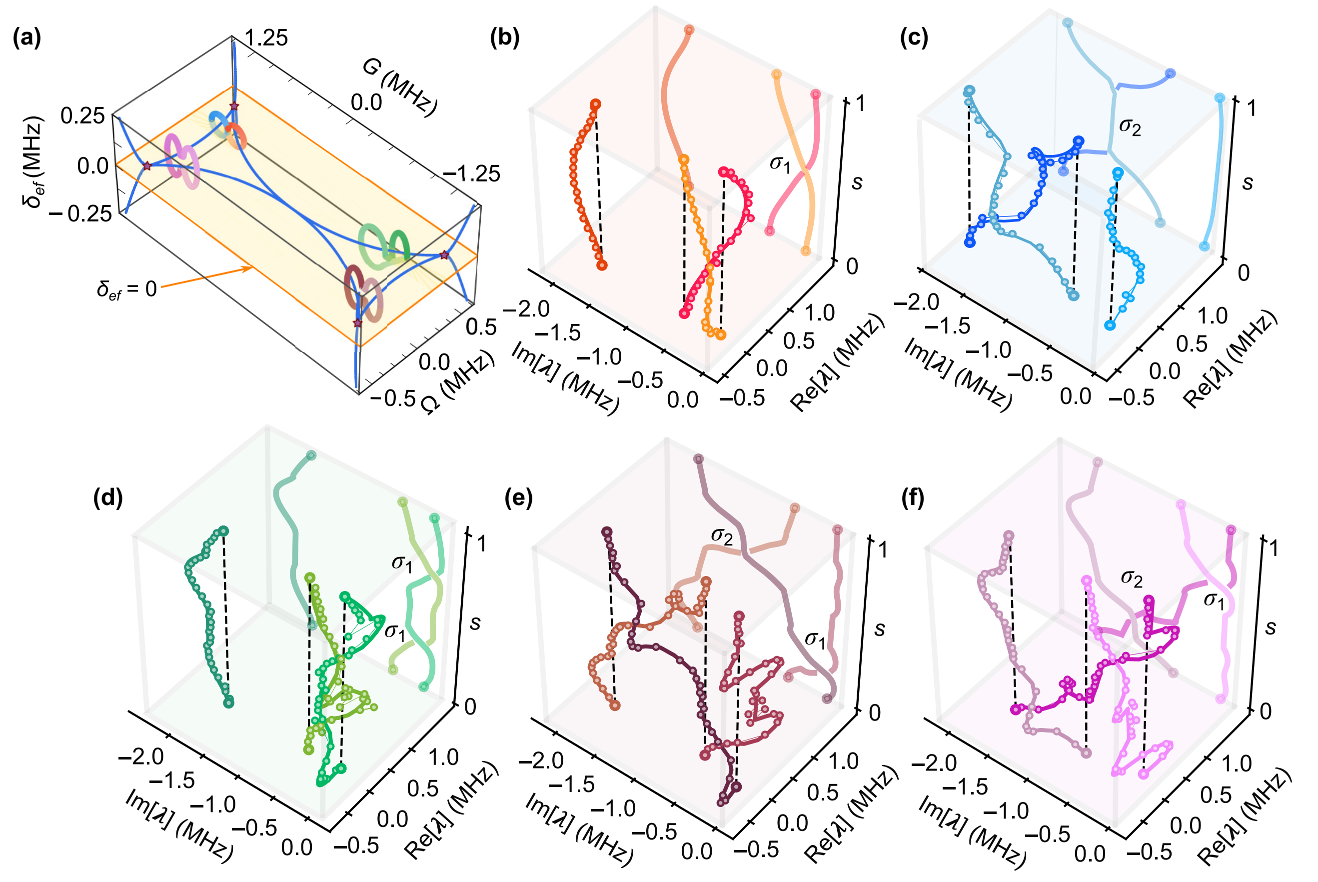

FIG. 3. Braid of eigenvalues. (a) EPs and control loops. Blue solid lines represent EPs. Red, blue, green, brown, and purple loops represent the control loops around EPs. Each loop is parameterized as $l(s)$ and completes a full cycle as s increases from 0 to 1. The yellow plane denotes the surface $\delta_{ef} = 0$, and the stars mark the four EP3s. (b)–(f) Braid of eigenvalues corresponding to the five control loops in (a). Dots represent the experiment data and solid lines indicate theoretic results. The standard error of the mean in the measured data is no larger than the size of the plotted points. The projected planes offer a front-view perspective of braids.

dynamical loops within the plane $G = 0.845$ MHz, which intersects with the exceptional arcs twice creating two EPs, as shown in Fig. 4(a). Each loop is a rectangle with a height of $2a$ and a width of $\Omega_m - \Omega_0$ where $a/2\pi = 5$ MHz is the maximum value of detuning and $\Omega_m = 5$ MHz is the fixed maximum value of Ω. The four edges of the rectangle are swept consecutively in either a clockwise (CW) or counterclockwise (CCW) direction at different constant velocities, ensuring that each edge is traversed in $T/4$ time, where T is the total period. The starting point of the loop is situated at $(\Omega_0, 0)$. By increasing the value of Ω_0, the loop is squeezed and the number of surrounding EPs decreases from two to zero.

Since the eigenstate is expressed in the basis involving the resonator's state, we develop an approach to prepare a specific initial state. To characterize the final state, we first perform standard quantum state tomography between the states $|e,0\rangle$ and $|f,0\rangle$. Then we continue the evolution without the *e*-*f* Rabi drive to extract the information about the $|g,1\rangle$ (see Appendix D). During the evolution, we dynamically adjust the phase of the *e*-*f* pulse to correct the unwanted phase shifts arising from changes in detuning.

To examine the exchange among the eigenstates along different loops, we prepare the initial state as the right eigenstate $|\psi_2\rangle$ and allow the system to evolve according to the loop, where $|\psi_j\rangle$ represents the jth normalized right eigenstate associated with the eigenvalue λ_j. Figures 4(b), 4(c), 4(f), and 4(g) show the simulation results of overlap $F_j = |\langle\psi_j|\psi(T)\rangle|^2$ between the normalized final state $|\psi(T)\rangle$ and the remaining right eigenstates $|\psi_1\rangle$ and $|\psi_3\rangle$. Different from the adiabatic limit ($T \to \infty$), the state transfer is strongly influenced by both the period T and the position of the starting point [33]. For the loops encompassing two EPs, the final state always transfers to the eigenstate $|\psi_3\rangle$ at some specific times regardless of the direction. Similar time-symmetric behaviors are also observed for the loops enclosing one EP. However, chiral-state transfer occurs when no EPs are surrounded by the loops. As indicated by the pink triangles in Figs. 4(b), 4(c), 4(f), and 4(g), the CW loop yields the transfer from $|\psi_2\rangle$ to $|\psi_3\rangle$, while the CCW loop causes the transfer from $|\psi_2\rangle$

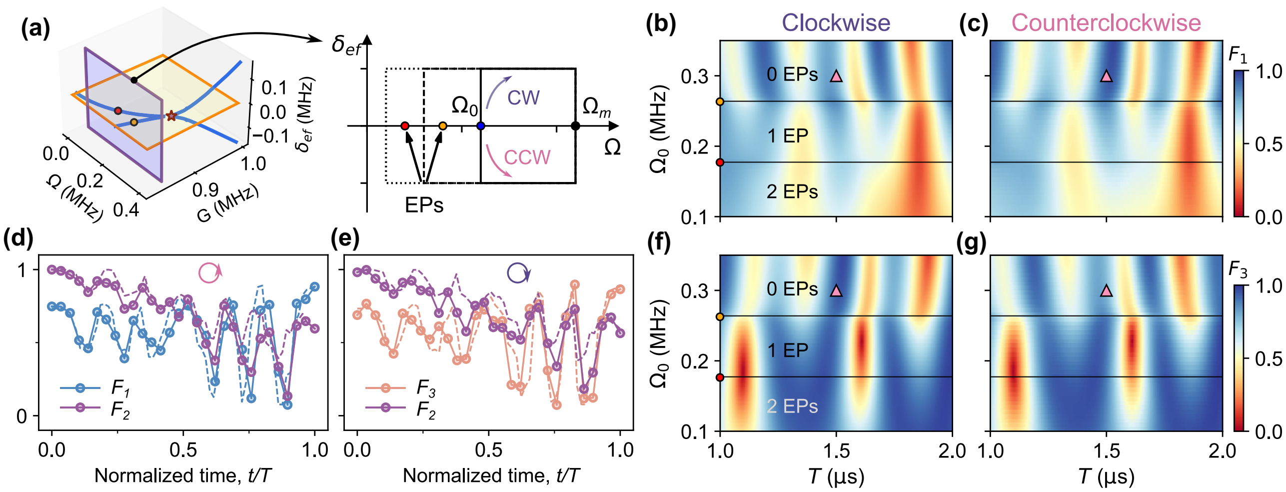

FIG. 4. Dynamically encircle EPs. (a) The sketch of encirclement loops on the plane $G = 0.845$ MHz. By adjusting the initial point $(\Omega_0, 0)$, the number of EPs encircled by the loop can be reduced from two to zero. The encirclement direction is either clockwise (CW) or counterclockwise (CCW). (b),(c) and (f),(g) The numerical results of state overlap $F_j = |\langle\psi_j|\psi(T)\rangle|^2$ over the encirclement period T and Ω_0 where $|\psi(t)\rangle$ is the normalized state at time t and $|\psi_j\rangle$ is the j-th normalized right eigenstate of initial Hamiltonian with $j = 1, 2$, and 3. The initial state is prepared at the right eigenstate $|\psi_2\rangle$. (d),(e) The state overlaps during the evolution using the parameter marked by the pink triangle in (b),(c) and (f),(g). The circles represent the experiment data and the dashed lines represent the numerical simulation results. The standard error of the mean in the measured data is no larger than the size of the plotted points.

to $|\psi_1\rangle$. Figures 4(d) and 4(e) plot the evolution of state overlap F_j over time in experiments using the parameters marked by the pink triangle. The experimental results are consistent with the numerical results. The oscillations in the overlaps during the evolution underline the importance of selecting an appropriate evolution time.

V. CONCLUSION AND DISCUSSION

We realize a non-Hermitian system containing an EP3 using superconducting circuits. We demonstrate that the EP3 is the intersection of multiple exceptional arcs. By identifying the exceptional arcs in the three-dimensional parameter space, we illustrate the generation of braid group B_3 by concatenating different classes of control loops. We also explore the chiral-state transfer between the eigenstates over a relatively short time by dynamically encircling the vicinity of the EP without enclosing it. Compared to the adiabatic approach, shortening the evolution time suppresses the decoherence effects of the device. We mention that the state transfer vanishes when the starting point is set at $(\Omega_m, 0)$, which highlights the role of the starting position [28].

The study of non-Hermitian systems can be greatly advanced through the flexibility and scalability of superconducting circuits. Beyond controlling coherent parameters, the dissipation rate can be enhanced by incorporating a Purcell filter without degrading the coherence of transmon [50,51], or dynamically tuned via a normal metal-insulator-superconductor tunnel junction [52,53]. By coupling multiple transmons, the composite system facilitates the exploration of entanglement generation near higher-order EPs [54] or enable Bell-state transfer between qubits [55]. The critical behaviors near the dynamic Mott transition, also identified as a *PT* symmetry-breaking transition [56,57], can be investigated using an array of superconducting islands [58–61]. This highlights the broad potential of superconducting electronics for exploring *PT* symmetry-breaking phenomena.

ACKNOWLEDGMENTS

This work was supported by the Innovation Program for Quantum Science and Technology (Grant No. 2021ZD0301800), the National Natural Science Foundation of China (Grants No. 12204528, No. 92265207, No. T2121001, No. 92065112), and Beijing Natural Science Foundation (Grant No. Z200009). This work also was supported by the Micro/nano Fabrication Laboratory of Synergetic Extreme Condition User Facility (SECUF). Devices were made at the Nanofabrication Facilities at the Institute of Physics, CAS in Beijing.

DATA AVAILABILITY

The data that support the findings of this article are not publicly available upon publication because it is not technically feasible and/or the cost of preparing, depositing, and hosting the data would be prohibitive within the terms of this research project. The data are available from the authors upon reasonable request.

APPENDIX A: SYMMETRIES OF NON-HERMITIAN HAMILTONIAN

Pseudochirality and anti-PT-symmetry are defined as $U_{\text{psCh}}HU_{\text{psCh}}^{-1} = -H^\dagger$ and $U_{\text{APT}}HU_{\text{APT}}^{-1} = -H^*$, respectively, where U_{psCh} and U_{APT} are two unitary operators and H represents the non-Hermitian Hamiltonian. The anti-PT-symmetry can be derived from the PT-symmetry by substituting $H \to iH$. By choosing

$$U_{\text{psCh}} = U_{\text{APT}} = \begin{pmatrix} 1 & 0 & 0 \\ 0 & -1 & 0 \\ 0 & 0 & 1 \end{pmatrix}, \tag{A1}$$

we can verify that the Hamiltonian in Eq. (1) preserves both symmetries when $\delta_{ef} = 0$. For a nonzero δ_{ef}, the eigenvalues of the Hamiltonian remain unchanged under the transformations $\Omega \to \Omega e^{i\phi}$ and $G \to Ge^{i\theta}$ by noticing that $U_1(\phi)H(\delta_{ef}, \Omega, G)U_1^{-1}(\phi) = H(\delta_{ef}, \Omega e^{i\phi}, G)$ and $U_2(\theta)H(\delta_{ef}, \Omega, G)U_2^{-1}(\theta) = H(\delta_{ef}, \Omega, Ge^{i\theta})$ where

$$U_1(\phi) = \begin{pmatrix} e^{i\phi} & 0 & 0 \\ 0 & 1 & 0 \\ 0 & 0 & 1 \end{pmatrix}, \tag{A2}$$

and

$$U_2(\theta) = \begin{pmatrix} 1 & 0 & 0 \\ 0 & 1 & 0 \\ 0 & 0 & e^{i\theta} \end{pmatrix}. \tag{A3}$$

APPENDIX B: METHOD FOR EXTRACTING EIGENVALUES

To extract eigenvalues of non-Hermitian Hamiltonian for each point in the trajectory, we initialize the system in the state $|\psi_0\rangle = (|e, 0\rangle - i|f, 0\rangle)/\sqrt{2}$ and measure the evolution of state probabilities P_e, P_f, and P_g. Here, P_g denotes the probability of the qutrit being in the state $|g\rangle$, irrespective of the resonator state.

The observed dynamics can be interpreted using the spectral decomposition of the non-Hermitian Hamiltonian $H = \sum_i \lambda_i |\psi_i^R\rangle\langle\psi_i^L|$ where $|\psi_i^R\rangle$ ($|\psi_i^L\rangle$) are the right (left) eigenstates of H, satisfying the bi-orthogonal condition $\langle\psi_i^L|\psi_j^R\rangle = \delta_{ij}$. This allows us to express the evolution of the state probability P_j for the state $|j\rangle$ as $P_j = \left|\sum_{i=1}^3 e^{-i\lambda_i t}\langle j|\psi_i^R\rangle\langle\psi_i^L|\psi_0\rangle\right|^2$. The explicit forms of right and left eigenstate are given by

$$|\psi_i^R\rangle = \left(\frac{-2G^2 + i\lambda\kappa + 2\lambda^2}{2G\Omega}, \frac{i\kappa + 2\lambda}{2G}, 1\right)^{\text{T}} \tag{B1}$$

and

$$|\psi_i^L\rangle = \left(\frac{G\Omega}{d(\lambda_i)}, \frac{-G(i\kappa/2 + \sum_{j\neq i}^3 \lambda_j)}{d(\lambda_i)}, \frac{c(\lambda_i)}{d(\lambda_i)}\right)^\dagger \tag{B2}$$

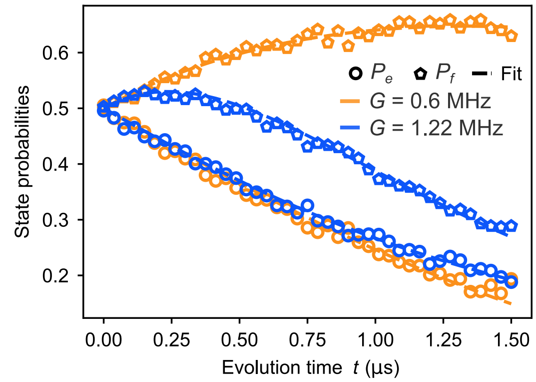

FIG. 5. Time evolution of state probabilities P_e and P_f.

with

$$c(\lambda_i) = G^2 - \kappa^2/4 + \frac{i\kappa}{2}\sum_{j\neq i}^3 \lambda_j + \prod_{j\neq i}^3 \lambda_j, \tag{B3}$$

$$d(\lambda_i) = \lambda_i^2 - \lambda_i \sum_{j\neq i}^3 \lambda_j + \prod_{j\neq i}^3 \lambda_j. \tag{B4}$$

The eigenvalues are functions of the parameters δ_{ef}, G, and Ω, as shown in Appendix J. Since $P_g = 1 - P_e - P_f$, we fit the measured evolution of P_e and P_f simultaneously to determine the unknown Hamiltonian parameters (δ_{ef}^{exp}, Ω^{exp}, G^{exp}), which are then used to calculate the eigenvalues. In Fig. 5, we present the evolution of state probabilities for two data points corresponding to $G = 0.6$ MHz and $G = 1.22$ MHz in Fig. 2(b) of the main text. Pentagon and circle markers denote the experimental data while the dashed lines represent the fitted results.

APPENDIX C: CONTROL LOOPS OF EIGENVALUE BRAIDING

The control loops shown in Fig. 3(a) consist of arcs and their corresponding straight-line segments. As shown in Fig. 6(a), both the red and blue loops are ellipses lying in the plane $\Omega = 0.25$ MHz while δ_{ef} and G are described by the following parametric equations:

$$\delta = \delta_r \sin(2\pi s), \tag{C1}$$

$$G = G_r \cos(2\pi s) + G_c, \tag{C2}$$

with $s \in [0, 1]$. Here, G_c represents the center of the ellipse along the $\delta_{ef} = 0$ axis, and $|\delta_r|$ and $|G_r|$ denote the height and width, respectively. The starting point also lies on the $\delta_{ef} = 0$ axis with $G = 1.17$ MHz. Both the red and blue loops share the same height $|\delta_r| = 0.05$ MHz and the same

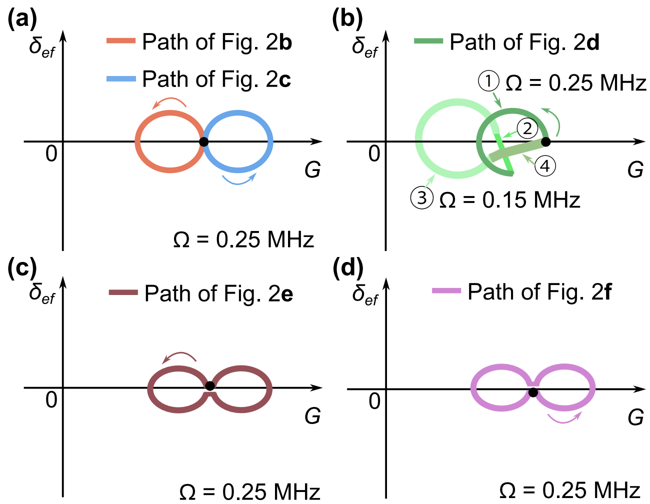

FIG. 6. The control loops corresponding to the eigenvalue braiding in Fig. 3.

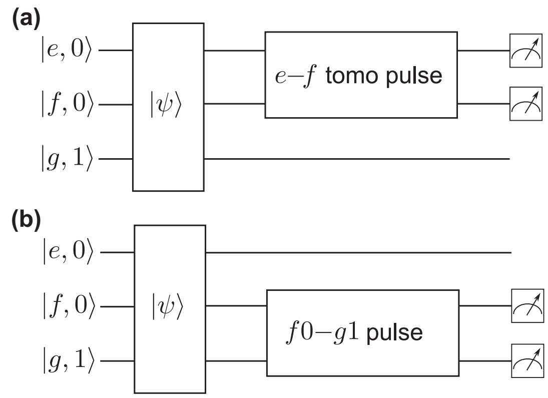

FIG. 7. State-tomography circuits for an unknown state $|\psi\rangle$ in two steps. (a) We apply the standard state-tomography pulses between $|e\rangle$ and $|f\rangle$ states. (b) We monitor the time evolution of P_f and P_g under a constant $f0$-$g1$ drive.

width $|G_r| = 0.11$ MHz. Meanwhile, the two branches of the EP2 arcs near EP3 penetrate the interiors of the red and blue loops, respectively, as shown in Fig. 3(a).

The other three loops in Fig. 3(a) each consist of two arcs connected by straight-line segments. The control loop corresponding to Fig. 3(d) follows a sequential path through four parts, labeled ①, ②, ③, and ④, as illustrated in Fig. 6(b). The first elliptical arc (①) lies in the plane $\Omega = 0.25$ MHz with the same starting point as in Fig. 3(a), while the second arc (③) is in the plane $\Omega = 0.15$ MHz. These two arcs are linked by two straight-line segments (②④). As shown in Fig. 3(a), the entire loop encircles the same EP2 branch twice and leads to the group element σ_1^2.

The remaining loops in Figs. 6(c) and 6(d) are composed of the same structural elements. The two elliptical arcs in Fig. 6(c) share the same height $|\delta_r| = 0.1$ MHz and width $|G_r| = 0.1$ MHz. The left and right arcs encircle different EP2 branches and are connected by two short horizontal straight lines. The entire loop is slightly shifted downward, positioning the staring point on the upper segment, with the loop first transversing the left arc. In contrast, the loop in Fig. 6(d) is slightly shifted upward, placing the starting point on the lower segment, with the loop first transversing the right arc. This difference in encirclement order thus results in two distinct group elements $\sigma_2\sigma_1$ and $\sigma_1\sigma_2$.

APPENDIX D: STATE TOMOGRAPHY OF EIGENSTATES

For an unknown state $|\psi\rangle = A|e,0\rangle + Be^{i\beta}|f,0\rangle + Ce^{i\gamma}|g,1\rangle$, we reconstruct the state by determining the state probabilities $|A|^2$, $|B|^2$, and $|C|^2$, along with the relative phase differences between $|e,0\rangle$ and $|f,0\rangle$ and between $|f,0\rangle$ and $|g,1\rangle$. Our approach involves two main steps.

First, we apply a series of short e-f tomography pulses and measure the resulting state probabilities P_e and P_f. We employ three e-f tomography pulses $\{I, R_x^{ef}(\pi/2), R_y^{ef}(\pi/2)\}$ where $R^{ef}{}_x(\theta) = \exp(-i\sigma_x^{ef}\theta/2)$ and $R^{ef}{}_y(\theta) = \exp(-i\sigma_y^{ef}\theta/2)$ with σ_x^{ef} and σ_y^{ef} being the Pauli operators defined between the states $|e\rangle$ and $|f\rangle$. The measured values of P_e and P_f then allow us to estimate $|A|^2$, $|B|^2$, and the phase factor $e^{i\beta}$ using maximum-likelihood estimation [62].

Second, we apply a constant $f0$-$g1$ drive and monitor the time evolution of the state probabilities P_f and P_g. Since our focus is on the final state of the dynamically encircling process on the $\Omega - \delta_{ef}$ plane under a fixed $f0$-$g1$ drive, all other parameters are set to zero except for the $f0$-$g1$ drive during this tomography phase. By fitting the observed evolution with the known coupling strength G and $|B|^2$, we can extract the probability $|C|^2$ and the relative phase $e^{i(\gamma-\beta)}$ between $|f,0\rangle$ and $|g,1\rangle$.

Figure 7 depicts the complete tomography circuit used for the state $|\psi\rangle$. Combining the information from both steps allows us to fully reconstruct the unknown state.

APPENDIX E: EXPERIMENTAL SETUP

Our experimental setup consists of a superconducting quantum processor with ten superconducting transmon qubits, each coupled to a dedicated microwave resonator. To control and characterize multiple qubits, we developed an electronic hardware system housed in a VPX-6U chassis, as shown in Fig. 8. This system includes multiple channels for arbitrary waveform generation (AWG), analog-to-digital conversion (ADC), and dc sources. The setup utilizes both longitudinal (Z control) and transverse (XY control) lines to deliver pulses that drive qubit evolution along the Z andXY directions. For Z control, energy level spacing adjustments are made using a combination

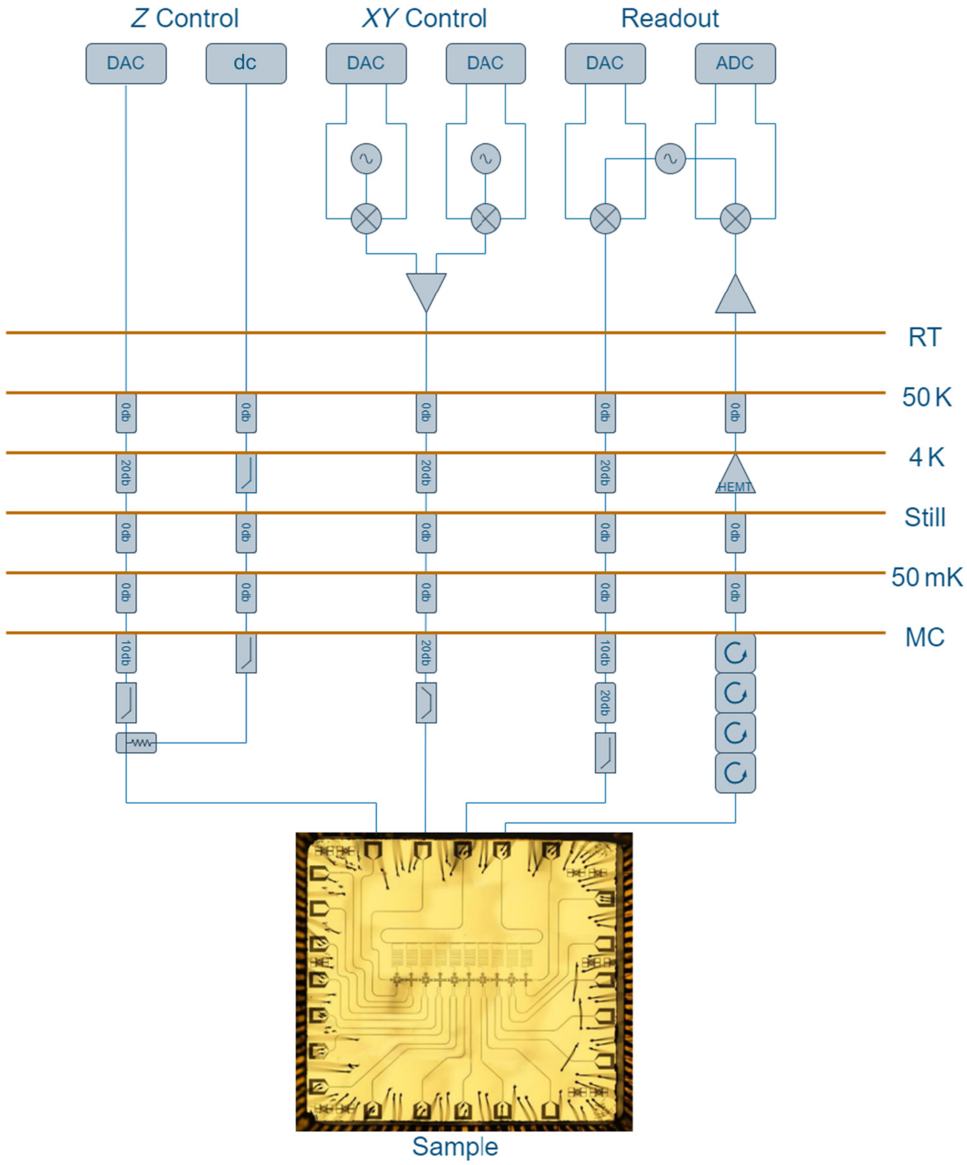

FIG. 8. Diagram of the quantum measurement and control system. A dilution refrigerator provides an ultralow temperature environment for the chip. The measurement and control system in the room-temperature environment interacts with the qubits by inputting and retrieving microwave signals.

of fast AWG bias and slow dc bias. For *XY* control, we employ two sets of AWG channels and microwave sources to create microwave pulses with precisely tuned frequencies, amplitudes, and phases, enabling manipulation of qubit states.

We exploit one qubit of the ten-qubit chain. The frequencies of dispersion readout cavities increase from 6.5 to 6.7 GHz with a step size of 20 MHz to economize the frequency space and achieve suitable detuning. By mixing the carrier signal generated from microwave source and the envelop signal generated from AWG channels, we can send resonant Rabi pulses through the *XY* line to drive the qubit's evolution between two specific energy levels. In our experiment, we consider the lowest three energy levels $|g\rangle$, $|e\rangle$, and $|f\rangle$ of transmon. A π_{ge} pulse excites the transmon from the $|g\rangle$ state to the $|e\rangle$ state, and a π_{ef} pulse excites the transmon from the $|e\rangle$ state to the $|f\rangle$ state, with respective driving frequencies of $\omega_{ge}/2\pi = 5.684$ GHz and $\omega_{ef}/2\pi = 5.431$ GHz.

The readout of qutrit state is achieved by utilizing dispersive measurement techniques due to $|\omega_r - \omega_{ge}| \gg J$ and $|\omega_r - \omega_{ef}| \gg J$. The readout probe tone with a duration of 2 μs is generated, shaped, and timed using heterodyne mixing like *XY* signals and sent down into the cryostat. The transmitted readout signal S_{21} is amplified, first in a HEMT amplifier and then in room-temperature

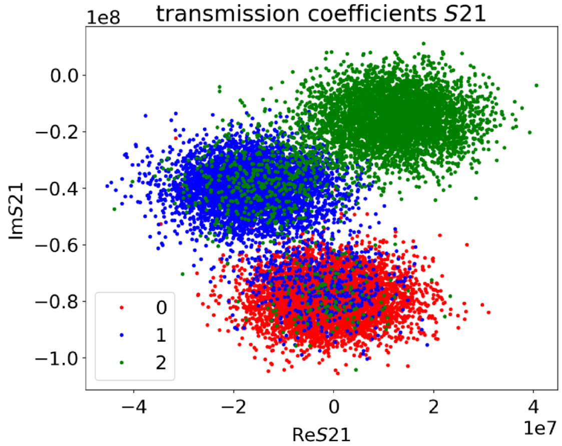

FIG. 9. Corresponding complex plane representation of the transmission coefficients S_{21}. We distinguish the readout signals corresponding to different states of the qutrit through single-shot experiments. Each point in the graph is composed of the in-phase and quadrature components of the S_{21} signal. The readout signals of the qutrit's three states can be effectively separated by optimizing the amplitudes and frequencies of readout pulses.

amplifiers. Next, the transmitted signal is down-converted using heterodyne mixing and finally sampled in a digitizer, acquiring the I and Q quadrature components. To establish an assignment rule that discriminates different transmon states, we compile reference data of 15 000 single-shot traces acquired with the transmon initialized in the states $|g\rangle$, $|e\rangle$, and $|f\rangle$. After optimizing the readout pulses' length, amplitudes, and frequencies, we can distinguish the qutrit states as shown in Fig. 9. Three clusters labeled by 0, 1, 2 in Fig. 9 correspond to energy levels $|g\rangle$, $|e\rangle$, and $|f\rangle$, which have readout fidelities of 98.88%, 89.2%, 86.84%. The readout fidelity is defined as the statistical probability of preparing one state and finally measuring the same state. We then use the assignment matrix P_{ij}, defined as the probability of observing the state $|i\rangle$ when the state $|j\rangle$ is prepared, to mitigate readout errors.

APPENDIX F: AC-STARK SHIFT CALIBRATION

An effective coupling between the transmon and the resonator can be achieved by applying coherent microwaves toned at specific frequencies. Since the drive between the states $|f,0\rangle$ and $|g,1\rangle$ acts on a second-order transition, it requires a high driving amplitude and results in significant ac-Stark shifts. In the experiment, taking this effect into account, we calibrate the transition π-pulses' frequencies under different $f0$-$g1$ pulses intensities to determine the shifts.

First, we calibrate the ac-Stark shift of $f0$-$g1$ transition. The experimental pulses are shown in Fig. 10(a). We first initialize the system in the ground state. Then, we apply two π sequent pulses, π_{ge} and π_{ef}, to prepare the system in the $|f,0\rangle$ state. Then, we apply a flattop waveform detection pulse with a frequency that varies near the $f0$-$g1$ transition frequency. Finally, we measure the evolved qutrit $|g\rangle$ state probability. We set the product of pulse intensity and pulse duration to a fixed and appropriate value, such that when the frequency of the driving pulse satisfies the resonance condition, the probability of the qutrit being in the $|g\rangle$ state after evolution is maximized. As shown in Fig. 10(c), through data processing, we obtain the corresponding relationship between the $f0$-$g1$ transition frequency and the $f0$-$g1$ driving intensity.

Similarly, we can then calibrate the detuning of the e-f pulse caused by the $f0$-$g1$ pulse. The experimental pulses are shown in Fig. 10(b). We first also initialize the system in the ground state. Then, we apply a π_{ge} pulse to prepare the system in the $|e,0\rangle$ state. Subsequently, we apply a flattop waveform detection pulse with a frequency that varies around the e-f transition and an experimental $f0$-$g1$ pulse. Finally, we measure the probability of the qutrit being in the $|e\rangle$ state. We specially set the time length and intensity of the e-f detection pulse to approximately generate a π pulse, while considering the impact of the $f0$-$g1$ transition on the $|e\rangle$ state probability, to achieve the highest transition fidelity. As before, we observe and calibrate a dependence of e-f transition frequency on the amplitude V_{f0g1} of the $f0$-$g1$ pulse as shown in Fig. 10(d).

APPENDIX G: CALIBRATION OF COUPLING STRENGTHS

After calibrating the ac-Stark shifts induced by the $f0$-$g1$ pulse, we can proceed to calibrate the coupling strengths Ω for the e-f transition and G for the $f0$-$g1$ transition. First, for the transition between the $|e\rangle$ and $|f\rangle$ states, the coupling strength is calibrated through the Rabi oscillation experiment. When the system is initially in the $|e\rangle$ state, the e-f drive causes the state $|e\rangle$ probability to oscillate periodically over time, as shown in Fig. 11(a). By fitting the evolution of the state probability $P(f)$ with the function $P_f(t) = \sin^2(\Omega t)$, we can obtain the relationship between the oscillating strength and driving intensity under this driving, as shown in Fig. 11(e). For the transition between the $|f,0\rangle$ and $|g,1\rangle$ states, we prepare the qutrit in the $|f\rangle$ state and then apply a resonant $f0$-$g1$ pulse. By fitting the evolution of the state probability $P(f)$ with the analytical expression $P_f(t) = e^{-\kappa t/2}|\cos(\gamma t) - \frac{\kappa}{4\gamma}\sin(\gamma t)|^2$ where $\gamma = \sqrt{G^2 - \kappa^2/16}$, we can obtain the corresponding coupling strength G and photon decay rate κ, as shown in Fig. 11(d). The calibration results are presented in Figs. 11(e) and 11(f). Finally, having obtained the corresponding relationships between the coupling strengths and AWG output amplitudes, we can accurately control the parameters Ω and G in the non-Hermitian Hamiltonian.

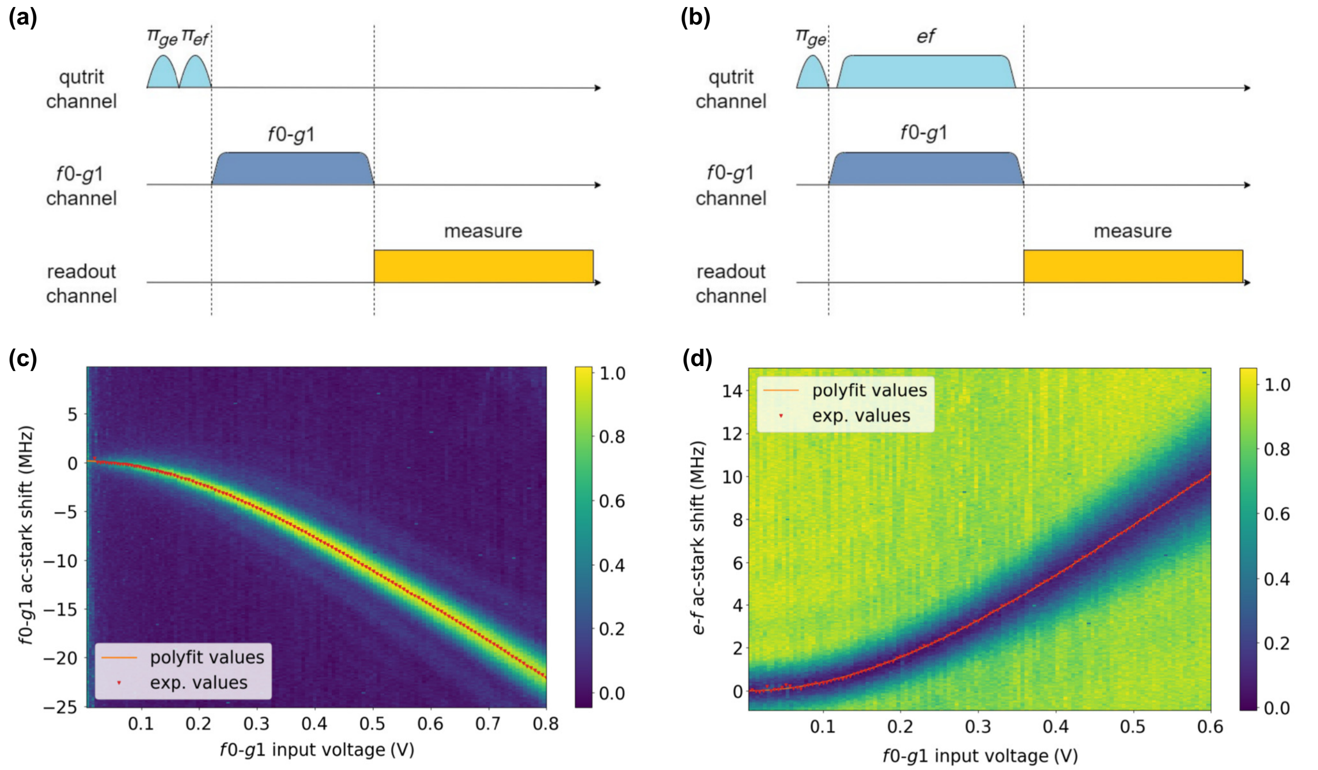

FIG. 10. The calibration of the ac-Stark effect. (a),(b) Illustration of the pulse schemes used to calibrate the ac-Stark effect. (c),(d) Measured result of ac-Stark shifts of $f0$-$g1$ transition and e-f transition versus the amplitude of the $f0$-$g1$ drive.

APPENDIX H: PREPARATION OF NON-HERMITIAN EIGENSTATES

We prepare the desired eigenstate through the following steps. Since the target state can be factored as

$$\begin{aligned}|\psi\rangle &= A|e,0\rangle + Be^{i\beta}|f,0\rangle + Ce^{i\gamma}|g,1\rangle \\ &= \left(\frac{A}{\sqrt{A^2+B^2}}|e,0\rangle + \frac{Be^{i\beta}}{\sqrt{A^2+B^2}}|f,0\rangle\right)\sqrt{A^2+B^2} \\ &\quad + Ce^{i\gamma}|g,1\rangle, \end{aligned} \tag{H1}$$

we first apply consecutively a π_{ge} pulse and a π_{ef} pulse turning the system from the $|g,0\rangle$ state to the $|f,0\rangle$ state. Then we apply an $f0$-$g1$ pulse turning the $|f,0\rangle$ state into the $\sqrt{A^2+B^2}|f,0\rangle + Ce^{i\gamma}|g,1\rangle$ state. To take the dissipation effect of $f0$-$g1$ pulse into account, the corresponding pulse length and amplitudes are solved from the numerical calculation with the known decay rate κ. Finally we apply an e-f pulse rotating the state $|f,0\rangle$ into the $A/(\sqrt{A^2+B^2})|e,0\rangle + (Be^{i\beta})/(\sqrt{A^2+B^2})|f,0\rangle$ state.

APPENDIX I: CONSTRUCTION OF THE EXPERIMENTAL NON-HERMITIAN HAMILTONIAN

The key ingredient in the non-Hermitian Hamiltonian is the $f0$-$g1$ coupling, which is induced by a second-order transition. By applying a coherent driving pulse with the frequency ω_d, the Hamiltonian for the coupled system can be expressed as

$$\begin{aligned} H_0 &= \delta_r a^\dagger a + \delta_q b^\dagger b + \frac{\alpha}{2} b^\dagger b^\dagger b b + J(ab^\dagger + ba^\dagger) \\ &\quad + \frac{\Omega_{f0g1}}{2} b + \frac{\Omega^*_{f0g1}}{2} b^\dagger, \end{aligned} \tag{I1}$$

where a represents the annihilation operator of the resonator, b represents the annihilation operator of the transmon, $\delta_r = \omega_r - \omega_d$ is the resonator-drive detuning, $\delta_q = \omega_{ge} - \omega_d$ is the transmon-drive detuning, J is the coupling strength between the resonator and the transmon, α is the nonlinear of the transmon, and Ω_{f0g1} is the driving amplitude. We further truncate the transmon operator at the second excited state $|f\rangle$. The coupling between the states $|g,0\rangle$ and $|f,1\rangle$ is activated if the driving frequency satisfies $\omega_d = 2\omega_{ge} + \alpha - \omega_r + \Delta_{f0g1}$ where Δ_{f0g1} is the induced ac-Stark shift. Assuming that the driving amplitude is far less than the coupling strength, we can treat the driving term perturbatively which yields the effective coupling strength $G = \frac{J\Omega_{f0g1}}{\sqrt{2}} \frac{\alpha}{\Delta(\Delta+\alpha)}$ with $\Delta = \omega_r - \omega_{ge}$. By adding another Rabi driving pulse with the amplitude Ω between the states $|e,0\rangle$ and $|f,0\rangle$, the effective Hamiltonian in the subspace V spanned by the states $|e,0\rangle$, $|f,0\rangle$,

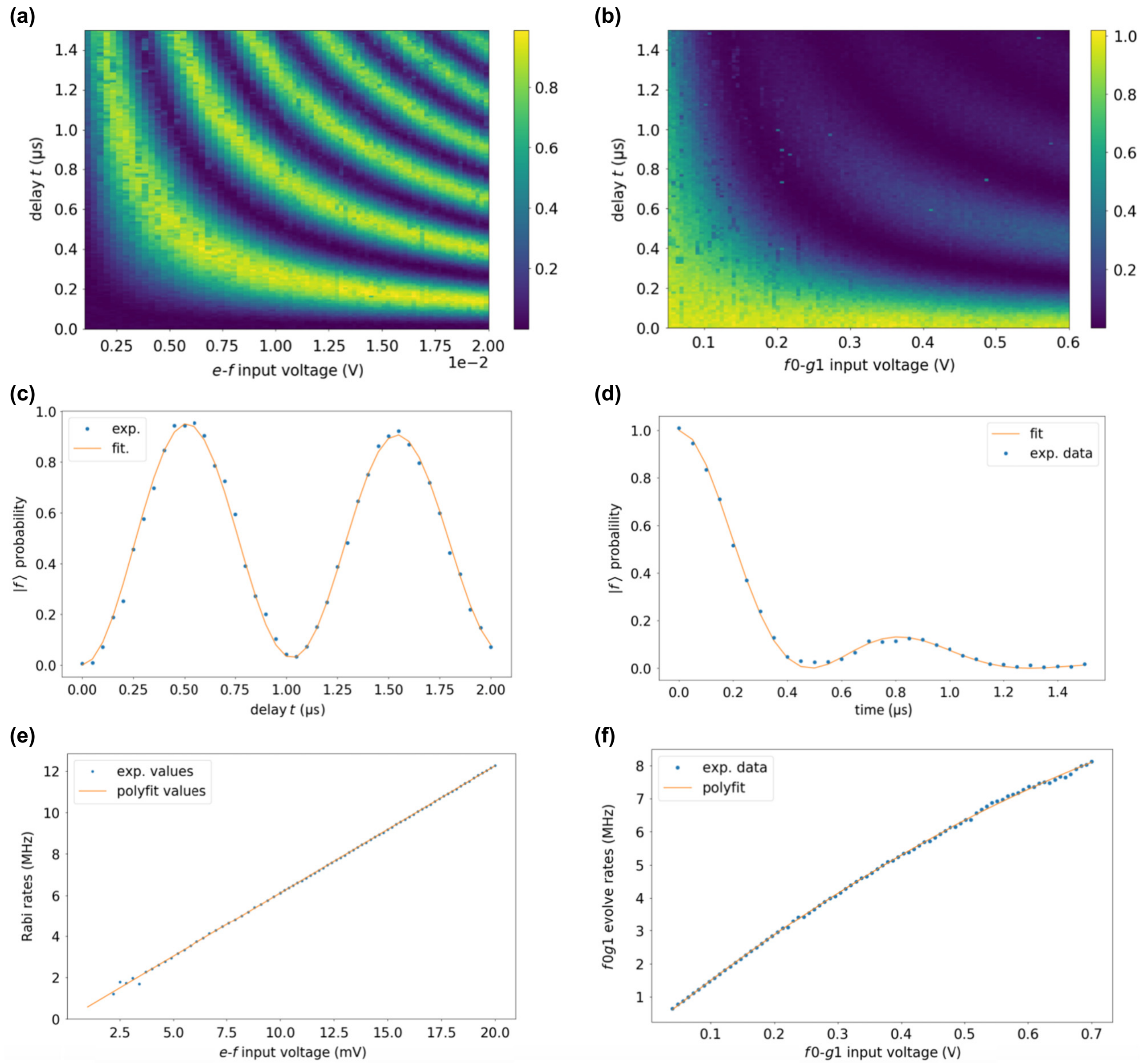

FIG. 11. The calibrations of the coupling strength. (a),(b) Calibration of the relationship between the coupling strengths Ω (for the transition between states $|e,0\rangle$ and $|f,0\rangle$) and G (for the transition between states $|f,0\rangle$ and $|g,1\rangle$) as a function of the AWG output amplitudes. (c),(d) Fitting of the evolution data to obtain the coupling strength. (e),(f) The coupling strength between states $|e,0\rangle$ and $|f,0\rangle$ exhibits a linear increase with the AWG output amplitude, while the oscillation strength between states $|f,0\rangle$ and $|g,1\rangle$ shows a quadratic dependence on the AWG output amplitude.

and $|g,1\rangle$ can be expressed as

$$\tilde{H} = \begin{pmatrix} -\delta_{ef} & \Omega & 0 \\ \Omega & 0 & G \\ 0 & G & 0 \end{pmatrix}, \tag{I2}$$

where δ_{ef} is the frequency detuning accounting for the ac-Stark shift induced by the $f0$-$g1$ pulse. Considering the decay of the state $|g,1\rangle$ to $|g,0\rangle$, the system's evolution can be described by the Lindblad master equation $\dot{\rho} = -i[\tilde{H},\rho] + \kappa\left(a\rho a^\dagger - \frac{1}{2}a^\dagger a\rho - \frac{1}{2}\rho a^\dagger a\right)$ where κ is the photon decay rate of the resonator. By restricting the dynamics to the subspace V, the effective system evolution is governed by a non-Hermitian Hamiltonian $H = \tilde{H} - i\kappa/2|g,1\rangle\langle g,1|$ as presented in Eq. (1).

APPENDIX J: EPS IN THE EXPERIMENTAL NON-HERMITIAN HAMILTONIAN

The eigenvalues of the non-Hermitian Hamiltonian are the roots of a cubic characteristic polynomial, which can be generally written as

$$\lambda^3 + m\lambda^2 + n\lambda + l = 0. \tag{J1}$$

Substituting $\lambda = t - m/3$ into Eq. (J1) yields a simpler cubic polynomial

$$t^3 + rt + s = 0, \tag{J2}$$

with $r = n - m^2/3$ and $s = l - mn/3 + 2m^3/27$. Assume that the root of Eq. (J2) can be expressed as $t = u + v$ and substituting this into Eq. (J2), we obtain $r = -3uv$ and $s = -(u^3 + v3)$. Multiplying v^3 both sides of the equation for s by v^3, we have a quadratic equation $v^6 + sv^3 - r^3/27 = 0$ in terms of v^3. The solution can be thus written as $v^3 = -s/2 + \sqrt{\Delta}$ and $u^3 = -s/2 - \sqrt{\Delta}$ where $\Delta = s^2/4 + r^3/27$ is the determinant. By denoting ω as $e^{i2\pi/3}$, the three roots λ_1, λ_2, and λ_3 can be expressed as

$$\lambda_1 = \left(-\frac{s}{2} + \sqrt{\Delta}\right)^{1/3} + \left(-\frac{s}{2} - \sqrt{\Delta}\right)^{1/3} - \frac{m}{3}, \tag{J3}$$

$$\lambda_2 = \left(-\frac{s}{2} + \sqrt{\Delta}\right)^{1/3} \omega + \left(-\frac{s}{2} - \sqrt{\Delta}\right)^{1/3} \omega^* - \frac{m}{3}, \tag{J4}$$

$$\lambda_3 = \left(-\frac{s}{2} + \sqrt{\Delta}\right)^{1/3} \omega^* + \left(-\frac{s}{2} - \sqrt{\Delta}\right)^{1/3} \omega - \frac{m}{3}. \tag{J5}$$

Therefore, all the three eigenvalues can be parameterized with two variables (s, Δ). When $\Delta = 0$, $\lambda_2 = \lambda_3$, corresponding to a second-order EP where two eigenvalues coalesce. When $\Delta = s = 0$, $\lambda_1 = \lambda_2 = \lambda_3$, corresponding to a third-order EP where all three eigenvalues coincide.

The characteristic polynomial of the non-Hermitian Hamiltonian in our work is given by

$$\varphi_H(\lambda) = \lambda^3 + \left(i\frac{\kappa}{2} + \delta_{ef}\right)\lambda^2 + \left(\frac{i\delta_{ef}\kappa}{2} - G^2 - \Omega^2\right)\lambda - G^2\delta_{ef} - \frac{i\Omega^2\kappa}{2}. \tag{J6}$$

By comparing with Eq. (J1), we obtain the expression of determinant Δ at $\delta_{ef} = 0$

$$\Delta = \frac{1}{432}\Big(-16G^6 + G^4\left(\kappa^2 - 48\Omega^2\right) - \Omega^2\left(\kappa^2 + 4\Omega^2\right)^2 + 4G^2\left(5\kappa^2\Omega^2 - 12\Omega^4\right)\Big), \tag{J7}$$

which specifies the boundary lines at the surface $\delta_{ef} = 0$ as shown in Fig. 2 of the main text. For the case $\delta_{ef} \neq 0$, the determinant is given by

$$\begin{aligned}46656\Delta = &-\left(12G^2 - \kappa^2 + 12\Omega^2 - 2i\kappa\delta_{ef} + 4\delta_{ef}^2\right)^3 \\ &- \Big(-18G^2\kappa + \kappa^3 + 36\kappa\Omega^2 \\ &- 3i\left(24G^2 - \kappa^2 - 12\Omega^2\right)\delta_{ef} \\ &+ 6\kappa\delta_{ef}^2 + 8i\delta_{ef}^3\Big)^2,\end{aligned} \tag{J8}$$

which specifies the exceptional lines in the three-dimensional parameter space in Fig. 3 of the main text. In addition to the curves shown in Fig. 3(a), we note the existence of two exceptional lines defined as $\{(\delta_{ef}, \Omega, G) | \Omega = 0, G = \pm\kappa/4\}$, which are not relevant to our results.

The EP3 is identified as the intersection of the two curves $s = 0$ and $\Delta = 0$. As shown in the main text, EP3 can only appear on the surface $\delta_{ef} = 0$ where $-i\kappa^3/108 - \frac{1}{2}i\kappa\Omega^2 - \frac{1}{6}i\kappa\left(-G^2 - \Omega^2\right)$. Using Eq. (J7), we derive four EP3 solutions given by $(G, \Omega) = (\pm\frac{1}{3}\sqrt{\frac{2}{3}}\kappa, \pm\frac{\kappa}{6\sqrt{3}})$.

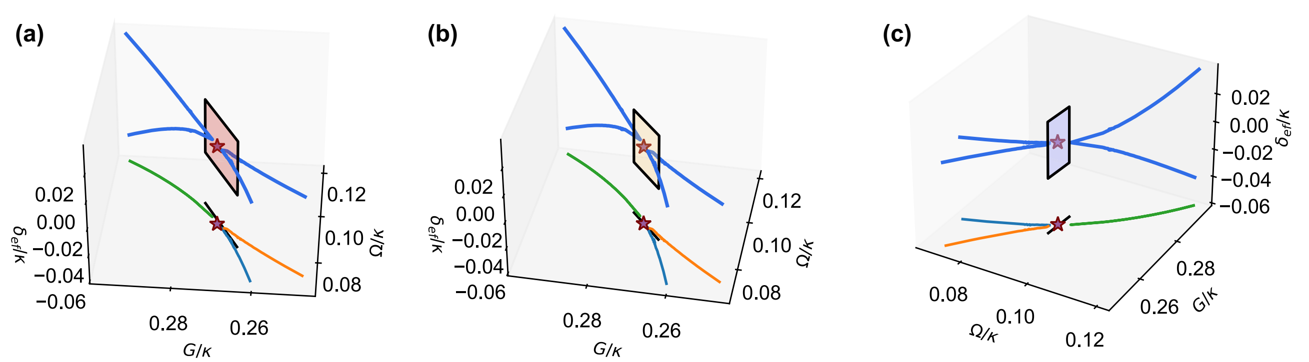

FIG. 12. Different encircling loops around the EP3. The blue arcs represent the exceptional arcs determined by Eq. (J8) in the three-dimensional parameter space. The red star denotes the EP3, which are encircled by the black loops. The black rectangles in (a)–(c) represent three loops, which cannot be smoothly deformed into each other without crossing exceptional lines. The projection of these encircling loops and exceptional arcs onto the bottom surface highlights the topological differences among the loops.

APPENDIX K: ANISOTROPY OF ENCIRCLING AN EP3

As demonstrated in the previous section, the EP3 resides at the intersection of exceptional arcs in the parameter space, imparting an anisotropic structure around it. Consequently, an encirclement of the EP3 can be classified in different ways. Figure 12 illustrates three representative encirclement cases around an EP3. In Fig. 12(a), the loop (black rectangle) encircling around the EP3 (red star) lies on the red plane, which divides the four exceptional arcs such that one part lies on one side of the plane and the remaining arcs on the opposite of the plane. This loop isolates one exceptional arc (represented by the yellow line) from the other three, effectively creating a path around only the yellow arc and resulting in a braid between two eigenvalues.

In Fig. 12(b), the loop is located on the yellow plane, which separates the blue arc from the remaining arcs. This configuration reduces to a loop only encircling an EP2, resulting in a braid between another set of two eigenvalues.

In Fig. 12(c), the loop lies on the blue plane, which divides the arcs into two equal groups, each containing two arcs (with two exceptional arcs projected onto the green arc). This loop can be regarded as encircling either of these two sets, producing a braid among three eigenvalues. Both perspectives must lead to the same braid which reveals another braid identity with the same form as the Yang-Baxter equation, as detailed in the next section.

APPENDIX L: VERIFICATION OF THE YANG-BAXTER EQUATION

Due to the intricate geometry of the parameter space near an EP3, a loop around the EP3 is equivalent to a sequence of loops around different exceptional lines, as shown in Fig. 13(a). The encirclement can be viewed in two ways: either as two successive loops around the exceptional arcs on the surface where $\delta_{ef} = 0$ [the figure pointed by the upper arrow in Fig. 13(a)] or as two successive loops around the exceptional arcs where $\delta_{ef} \neq 0$ [the figure pointed by the lower arrow in Fig. 13(a)].

For the first decomposition, the two loops lead to two eigenvalue braids, as shown in Figs. 13(b) and 13(c), which correspond to the braid elements σ_1 and σ_2 in the braid group B_3, respectively. In the second decomposition, the loops produce two eigenvalue braids, as shown in Figs. 13(d) and 13(e), which can be described by the braid element $\sigma_2\sigma_1\sigma_2^{-1}$ and σ_1, respectively. Since both types of decompositions can be continuously deformed to represent an EP3 encirclement, we obtain the following identity:

$$\sigma_2\sigma_1 = \sigma_1\sigma_2\sigma_1\sigma_2^{-1}, \tag{L1}$$

which is a form of the Yang-Baxter equation

$$\sigma_2\sigma_1\sigma_2 = \sigma_1\sigma_2\sigma_2. \tag{L2}$$

APPENDIX M: COMPENSATED PHASES DURING DYNAMICAL ENCIRCLEMENT OF EPS

We dynamically encircle EPs by varying the driving frequency and amplitude of the *e*-*f* pulse. Since the driving frequency is a piecewise function of time, we compensate for the phases between two adjacent segments. We slice the total evolution into N segments separated by times $\{t_0, t_1, \ldots, t_N\}$. Both amplitude and frequency remain constant within each segment. The driving phase is compensated at the beginning of each new segment. We start with the first segment. The Hamiltonian in the lab frame can be written as

$$H_1 = -\frac{1}{2}\omega_s\sigma^z + \left(\sigma^+\Omega_1(t)e^{-i\omega_1 t} + \text{H.c.}\right), \tag{M1}$$

where ω_s is the transition frequency between the two states, ω_1 is the driving frequency, and $\Omega_1(t)$ is the driving amplitude. In a rotating frame to remove the oscillation terms,

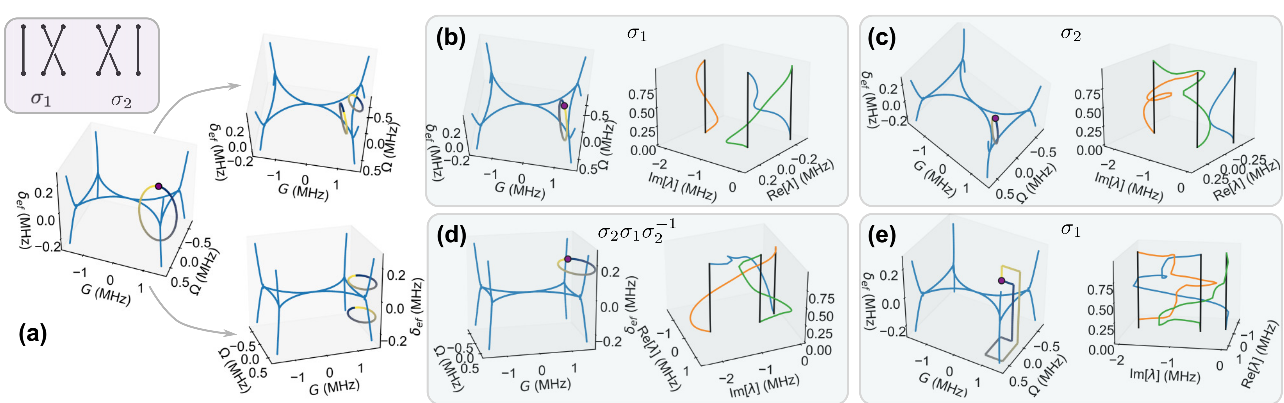

FIG. 13. Yang-Baxter equation. (a) Illustration of two possible decompositions for an EP3 encirclement. (b),(c) Eigenvalue braids resulting from the first decomposition. (d),(e) Eigenvalue braids resulting from the second decomposition.

the Hamiltonian is given by

$$\tilde{H}_1 = -\frac{1}{2}\delta_1\sigma^z + \left(\Omega_1(t)\sigma^+ + \text{H.c.}\right), \quad \text{(M2)}$$

where $\delta_1 = \omega_s - \omega_1$. Assume that the initial state at time t_0 is $|\varphi_0\rangle$. Then the state at t_1 in the lab coordinate can be expressed as

$$|\psi(t_1)\rangle = R_z(\omega_1\Delta t_1)|\varphi(t_1)\rangle, \quad \text{(M3)}$$

$$|\varphi(t_1)\rangle = e^{-i\mathbb{T}\int_0^{\Delta t_1}\tilde{H}_1(\tau)d\tau}|\varphi_0\rangle, \quad \text{(M4)}$$

where $R_z(\phi) \equiv e^{-i\phi\sigma^z/2}$, $|\varphi(t_1)\rangle$ is the state at t_1 in the rotating frame, $\Delta t_1 = t_1 - t_0$, and $\mathbb{T}$ is the time-ordering operator. By replacing $\Omega_1(t)$ with $\Omega_2(t)$ to evolve from t_1 and t_2 with a new driving frequency ω_2, the state at t_2 in the rotating frame is expected to be

$$|\varphi(t_2)\rangle = e^{-i\mathbb{T}\int_0^{\Delta t_2}\tilde{H}_2(\tau)d\tau}|\varphi(t_1)\rangle, \quad \text{(M5)}$$

with $\Delta t_2 = t_2 - t_1$ and $\tilde{H}_2 = -\frac{1}{2}\delta_2\sigma^z + (\Omega_2(t)\sigma^+ + \text{H.c.})$. By adding a phase ϕ_1 to $\Omega_2(t)$ at time t_1, the state at t_2 in the lab frame is

$$\begin{aligned} |\psi(t_2)\rangle &= R_z(\omega_2\Delta t_2)|\varphi(t_2)\rangle \\ &= R_z(\omega_2\Delta t_2)R_z(\phi_1)e^{-i\mathbb{T}\int_0^{\Delta t_2}\tilde{H}_2 d\tau}R_z^\dagger(\phi_1)|\psi(t_1)\rangle. \end{aligned} \quad \text{(M6)}$$

Therefore, the additional ϕ_1 can be chosen as

$$\phi_1 = \omega_1\Delta t_1 \quad \text{(M7)}$$

to eliminate the unwanted dynamical phase term $R_z(\omega_1\Delta t_1)$. Similarly, if we apply another driving pulse of a duration Δt_3 in the driving frequency ω_3, the additional phase ϕ_2 at t_2 satisfies

$$\phi_2 = \omega_2\Delta t_2 + \phi_1 = \omega_2\Delta t_2 + \omega_1\Delta t_1 \quad \text{(M8)}$$

to offset the phase term $R_z(\omega_2\Delta t_2)R_z(\phi_1)$. Generally, the compensated phase at time t_1 is given by

$$\phi_i = \sum_{j\le i}\omega_j\Delta t_j. \quad \text{(M9)}$$

[1] Z. Lin, H. Ramezani, T. Eichelkraut, T. Kottos, H. Cao, and D. N. Christodoulides, Unidirectional invisibility induced by $\mathcal{PT}$-symmetric periodic structures, Phys. Rev. Lett. **106**, 213901 (2011).

[2] L. Feng, Y.-L. Xu, W. S. Fegadolli, M.-H. Lu, J. E. B. Oliveira, V. R. Almeida, Y.-F. Chen, and A. Scherer, Experimental demonstration of a unidirectional reflectionless parity-time metamaterial at optical frequencies, Nat. Mater. **12**, 108 (2012).

[3] Y. Sun, W. Tan, H.-q. Li, J. Li, and H. Chen, Experimental demonstration of a coherent perfect absorber with PT phase transition, Phys. Rev. Lett. **112**, 143903 (2014).

[4] W. R. Sweeney, C. W. Hsu, S. Rotter, and A. D. Stone, Perfectly absorbing exceptional points and chiral absorbers, Phys. Rev. Lett. **122**, 093901 (2019).

[5] B. Peng, Ş. K. Özdemir, S. Rotter, H. Yilmaz, M. Liertzer, F. Monifi, C. M. Bender, F. Nori, and L. Yang, Loss-induced suppression and revival of lasing, Science **346**, 328 (2014).

[6] L. Feng, Z. J. Wong, R.-M. Ma, Y. Wang, and X. Zhang, Single-mode laser by parity-time symmetry breaking, Science **346**, 972 (2014).

[7] H. Hodaei, M.-A. Miri, M. Heinrich, D. N. Christodoulides, and M. Khajavikhan, Parity-time–symmetric microring lasers, Science **346**, 975 (2014).

[8] C. Wang, J. Rao, Z. Chen, K. Zhao, L. Sun, B. Yao, T. Yu, Y.-P. Wang, and W. Lu, Enhancement of magnonic frequency combs by exceptional points, Nat. Phys. **20**, 1139 (2024).

[9] K. G. Makris, R. El-Ganainy, D. N. Christodoulides, and Z. H. Musslimani, Beam dynamics in $\mathcal{PT}$ symmetric optical lattices, Phys. Rev. Lett. **100**, 103904 (2008).

[10] T. Kato, *Perturbation Theory for Linear Operators* (Springer Berlin, Heidelberg, 1995).

[11] Y. Ashida, Z. Gong, and M. Ueda, Non-Hermitian physics, Adv. Phys. **69**, 249 (2020).

[12] K. Wang, A. Dutt, C. C. Wojcik, and S. Fan, Topological complex-energy braiding of non-Hermitian bands, Nature **598**, 59 (2021).

[13] C. Guria, Q. Zhong, S. K. Ozdemir, Y. S. S. Patil, R. El-Ganainy, and J. G. E. Harris, Resolving the topology of encircling multiple exceptional points, Nat. Commun. **15**, 1369 (2024).

[14] C. C. Wojcik, X.-Q. Sun, T. Bzdušek, and S. Fan, Homotopy characterization of non-Hermitian Hamiltonians, Phys. Rev. B **101**, 205417 (2020).

[15] Z. Li and R. S. K. Mong, Homotopical characterization of non-Hermitian band structures, Phys. Rev. B **103**, 155129 (2021).

[16] H. Hu and E. Zhao, Knots and non-Hermitian Bloch bands, Phys. Rev. Lett. **126**, 010401 (2021).

[17] Y. S. S. Patil, J. Höller, P. A. Henry, C. Guria, Y. Zhang, L. Jiang, N. Kralj, N. Read, and J. G. E. Harris, Measuring the knot of non-Hermitian degeneracies and non-commuting braids, Nature **607**, 271 (2022).

[18] W. Tang, K. Ding, and G. Ma, Realization and topological properties of third-order exceptional lines embedded in exceptional surfaces, Nat. Commun. **14**, 6660 (2023).

[19] Y. Wu, Y. Wang, X. Ye, W. Liu, Z. Niu, C.-K. Duan, Y. Wang, X. Rong, and J. Du, Third-order exceptional line in a nitrogen-vacancy spin system, Nat. Nanotechnol. **19**, 160 (2024).

[20] R. Uzdin, A. Mailybaev, and N. Moiseyev, On the observability and asymmetry of adiabatic state flips generated by

exceptional points, J. Phys. A: Math. Theor. **44**, 435302 (2011).

[21] I. Gilary, A. A. Mailybaev, and N. Moiseyev, Time-asymmetric quantum-state-exchange mechanism, Phys. Rev. A **88**, 010102 (2013).

[22] T. J. Milburn, J. Doppler, C. A. Holmes, S. Portolan, S. Rotter, and P. Rabl, General description of quasiadiabatic dynamical phenomena near exceptional points, Phys. Rev. A **92**, 052124 (2015).

[23] A. U. Hassan, B. Zhen, M. Soljačić, M. Khajavikhan, and D. N. Christodoulides, Dynamically encircling exceptional points: Exact evolution and polarization state conversion, Phys. Rev. Lett. **118**, 093002 (2017).

[24] J. Feilhauer, A. Schumer, J. Doppler, A. A. Mailybaev, J. Böhm, U. Kuhl, N. Moiseyev, and S. Rotter, Encircling exceptional points as a non-Hermitian extension of rapid adiabatic passage, Phys. Rev. A **102**, 040201 (2020).

[25] H. Xu, D. Mason, L. Jiang, and J. G. E. Harris, Topological energy transfer in an optomechanical system with exceptional points, Nature **537**, 80 (2016).

[26] J. Doppler, A. A. Mailybaev, J. Böhm, U. Kuhl, A. Girschik, F. Libisch, T. J. Milburn, P. Rabl, N. Moiseyev, and S. Rotter, Dynamically encircling an exceptional point for asymmetric mode switching, Nature **537**, 76 (2016).

[27] J. W. Yoon, Y. Choi, C. Hahn, G. Kim, S. H. Song, K.-Y. Yang, J. Y. Lee, Y. Kim, C. S. Lee, J. K. Shin, H.-S. Lee, and P. Berini, Time-asymmetric loop around an exceptional point over the full optical communications band, Nature **562**, 86 (2018).

[28] X.-L. Zhang, S. Wang, B. Hou, and C. T. Chan, Dynamically encircling exceptional points: In situ control of encircling loops and the role of the starting point, Phys. Rev. X **8**, 021066 (2018).

[29] X.-L. Zhang and C. T. Chan, Dynamically encircling exceptional points in a three-mode waveguide system, Commun. Phys. **2**, 63 (2019).

[30] A. Schumer, Y. G. N. Liu, J. Leshin, L. Ding, Y. Alahmadi, A. U. Hassan, H. Nasari, S. Rotter, D. N. Christodoulides, P. LiKamWa, and M. Khajavikhan, Topological modes in a laser cavity through exceptional state transfer, Science **375**, 884 (2022).

[31] H. Nasari, G. Lopez-Galmiche, H. E. Lopez-Aviles, A. Schumer, A. U. Hassan, Q. Zhong, S. Rotter, P. LiKamWa, D. N. Christodoulides, and M. Khajavikhan, Observation of chiral state transfer without encircling an exceptional point, Nature **605**, 256 (2022).

[32] W. Liu, Y. Wu, C.-K. Duan, X. Rong, and J. Du, Dynamically encircling an exceptional point in a real quantum system, Phys. Rev. Lett. **126**, 170506 (2021).

[33] M. Abbasi, W. Chen, M. Naghiloo, Y. N. Joglekar, and K. W. Murch, Topological quantum state control through exceptional-point proximity, Phys. Rev. Lett. **128**, 160401 (2022).

[34] A. U. Hassan, G. L. Galmiche, G. Harari, P. LiKamWa, M. Khajavikhan, M. Segev, and D. N. Christodoulides, Chiral state conversion without encircling an exceptional point, Phys. Rev. A **96**, 052129 (2017).

[35] M. Pechal, L. Huthmacher, C. Eichler, S. Zeytinoğlu, A. A. Abdumalikov, S. Berger, A. Wallraff, and S. Filipp, Microwave-controlled generation of shaped single photons in circuit quantum electrodynamics, Phys. Rev. X **4**, 041010 (2014).

[36] S. Zeytinoğlu, M. Pechal, S. Berger, A. A. Abdumalikov, A. Wallraff, and S. Filipp, Microwave-induced amplitude- and phase-tunable qubit-resonator coupling in circuit quantum electrodynamics, Phys. Rev. A **91**, 043846 (2015).

[37] P. Magnard, P. Kurpiers, B. Royer, T. Walter, J.-C. Besse, S. Gasparinetti, M. Pechal, J. Heinsoo, S. Storz, A. Blais, and A. Wallraff, Fast and unconditional all-microwave reset of a superconducting qubit, Phys. Rev. Lett. **121**, 060502 (2018).

[38] J. Koch, T. M. Yu, J. Gambetta, A. A. Houck, D. I. Schuster, J. Majer, A. Blais, M. H. Devoret, S. M. Girvin, and R. J. Schoelkopf, Charge-insensitive qubit design derived from the Cooper pair box, Phys. Rev. A **76**, 042319 (2007).

[39] W. Tang, X. Jiang, K. Ding, Y.-X. Xiao, Z.-Q. Zhang, C. T. Chan, and G. Ma, Exceptional nexus with a hybrid topological invariant, Science **370**, 1077 (2020).

[40] I. Mandal and E. J. Bergholtz, Symmetry and higher-order exceptional points, Phys. Rev. Lett. **127**, 186601 (2021).

[41] P. Delplace, T. Yoshida, and Y. Hatsugai, Symmetry-protected multifold exceptional points and their topological characterization, Phys. Rev. Lett. **127**, 186602 (2021).

[42] P. Peng, W. Cao, C. Shen, W. Qu, J. Wen, L. Jiang, and Y. Xiao, Anti-parity–time symmetry with flying atoms, Nat. Phys. **12**, 1139 (2016).

[43] Y. Choi, C. Hahn, J. W. Yoon, and S. H. Song, Observation of an anti-PT-symmetric exceptional point and energy-difference conserving dynamics in electrical circuit resonators, Nat. Commun. **9**, 2182 (2018).

[44] Y. Li, Y.-G. Peng, L. Han, M.-A. Miri, W. Li, M. Xiao, X.-F. Zhu, J. Zhao, A. Alù, S. Fan, and C.-W. Qiu, Anti–parity-time symmetry in diffusive systems, Science **364**, 170 (2019).

[45] Y. Yang, Y.-P. Wang, J. W. Rao, Y. S. Gui, B. M. Yao, W. Lu, and C.-M. Hu, Unconventional singularity in anti-parity-time symmetric cavity magnonics, Phys. Rev. Lett. **125**, 147202 (2020).

[46] A. Bergman, R. Duggan, K. Sharma, M. Tur, A. Zadok, and A. Alù, Observation of anti-parity-time-symmetry, phase transitions and exceptional points in an optical fibre, Nat. Commun. **12**, 486 (2021).

[47] C. N. Yang and M. L. Ge, *Braid Group, Knot Theory and Statistical Mechanics* (World Scientific, Singapore, 1991).

[48] Z. Yang, A. P. Schnyder, J. Hu, and C.-K. Chiu, Fermion doubling theorems in two-dimensional non-Hermitian systems for Fermi points and exceptional points, Phys. Rev. Lett. **126**, 086401 (2021).

[49] W. Tang, K. Ding, and G. Ma, Direct measurement of topological properties of an exceptional parabola, Phys. Rev. Lett. **127**, 034301 (2021).

[50] E. Jeffrey, D. Sank, J. Y. Mutus, T. C. White, J. Kelly, R. Barends, Y. Chen, Z. Chen, B. Chiaro, A. Dunsworth, A. Megrant, P. J. J. O'Malley, C. Neill, P. Roushan, A. Vainsencher, J. Wenner, A. N. Cleland, and J. M. Martinis, Fast accurate state measurement with superconducting qubits, Phys. Rev. Lett. **112**, 190504 (2014).

[51] E. A. Sete, J. M. Martinis, and A. N. Korotkov, Quantum theory of a bandpass Purcell filter for qubit readout, Phys. Rev. A **92**, 012325 (2015).

[52] K. Y. Tan, M. Partanen, R. E. Lake, J. Govenius, S. Masuda, and M. Möttönen, Quantum-circuit refrigerator, Nat. Commun. **8**, 15189 (2017).

[53] M. Partanen, J. Goetz, K. Y. Tan, K. Kohvakka, V. Sevriuk, R. E. Lake, R. Kokkoniemi, J. Ikonen, D. Hazra, A. Mäkinen, E. Hyyppä, L. Grönberg, V. Vesterinen, M. Silveri, and M. Möttönen, Exceptional points in tunable superconducting resonators, Phys. Rev. B **100**, 134505 (2019).

[54] Z.-Z. Li, W. Chen, M. Abbasi, K. W. Murch, and K. B. Whaley, Speeding up entanglement generation by proximity to higher-order exceptional points, Phys. Rev. Lett. **131**, 100202 (2023).

[55] S. Khandelwal, W. Chen, K. W. Murch, and G. Haack, Chiral Bell-state transfer via dissipative Liouvillian dynamics, Phys. Rev. Lett. **133**, 070403 (2024).

[56] R. Hanai and P. B. Littlewood, Critical fluctuations at a many-body exceptional point, Phys. Rev. Res. **2**, 033018 (2020).

[57] V. Tripathi, A. Galda, H. Barman, and V. M. Vinokur, Parity-time symmetry-breaking mechanism of dynamic Mott transitions in dissipative systems, Phys. Rev. B **94**, 041104 (2016).

[58] N. Poccia, T. I. Baturina, F. Coneri, C. G. Molenaar, X. R. Wang, G. Bianconi, A. Brinkman, H. Hilgenkamp, A. A. Golubov, and V. M. Vinokur, Critical behavior at a dynamic vortex insulator-to-metal transition, Science **349**, 1202 (2015).

[59] I. Roy, P. Chauhan, H. Singh, S. Kumar, J. Jesudasan, P. Parab, R. Sensarma, S. Bose, and P. Raychaudhuri, Dynamic transition from Mott-like to metal-like state of the vortex lattice in a superconducting film with a periodic array of holes, Phys. Rev. B **95**, 054513 (2017).

[60] M. Lankhorst, N. Poccia, M. P. Stehno, A. Galda, H. Barman, F. Coneri, H. Hilgenkamp, A. Brinkman, A. A. Golubov, V. Tripathi, T. I. Baturina, and V. M. Vinokur, Scaling universality at the dynamic vortex Mott transition, Phys. Rev. B **97**, 020504 (2018).

[61] Z.-X. Pei, W.-G. Guo, and X.-G. Qiu, Dynamic vortex Mott transition in triangular superconducting arrays, Chin. Phys. B **31**, 037404 (2022).

[62] D. F. V. James, P. G. Kwiat, W. J. Munro, and A. G. White, Measurement of qubits, Phys. Rev. A **64**, 052312 (2001).